Deep learning with synthetic diffusion MRI data for free-water elimination in glioblastoma cases

Miguel Molina-Romero[1,2 [0000−0001−8054−0426]], Benedikt Wiestler[3 [0000−0002−2963−7772]], Pedro A. Gómez[1,2 [0000−0003−3709−3557]], Marion I. Menzel[2 [0000−0003−0087−9134]], and Bjoern H. Menze[1 [0000−0003−4136−5690]]

[1] Computer Science, Technischen Universität München, Munich, Germany
[2] GE Healthcare Global Research Organization, Munich, Germany
[3] Department of Neuroradiology, Klinikum rechts der Isar der Technischen Universität München, Munich, Germany.

Abstract. Glioblastoma is the most common and aggressive brain tumor. In clinical practice, diffusion MRI (dMRI) enables tumor infiltration assessment, tumor recurrence prognosis, and identification of white-matter tracks close to the resection volume. However, the vasogenic edema (free-water) surrounding the tumor causes partial volume contamination, which induces a bias in the estimates of the diffusion properties and limits the clinical utility of dMRI.
We introduce a voxel-based deep learning method to map and correct free-water partial volume contamination in dMRI. Our model learns from synthetically generated data a non-parametric forward model that maps free-water partial volume contamination to volume fractions. This is independent of the diffusion protocol and can be used retrospectively. We show its benefits in glioblastoma cases: first, a gain of statistical power; second, quantification of free-water and tissue volume fractions; and third, correction of free-water contaminated diffusion metrics. Free-water elimination yields more relevant information from the available data.

Keywords: Glioblastoma, Brain Tumor, DTI, Deep learning, Fractional Anisotropy, Free-water elimination, Data harmonization.

1 Introduction

Glioblastomas are the most common primary brain tumor. Ninety percent of these are IDH-wild-type and have a dismal prognosis, with a 5-year survival rate of less than 10%. Diffusion magnetic resonance imaging (dMRI) and the diffusion tensor model (DTI) are used clinically for surgical planing. DTI yields quantitative estimates of the tissue diffusivity, e.g. mean diffusivity (MD), and fractional anisotropy (FA), an index of tissue microstructure organization. Previous research focused on FA as indicator of tumor grade, tumor cellularity, tumor infiltration and edema assessment [1], and tumor recurrence [2]. However, results are controversial due to reproducibility issues derived from differences in methology, image acquisition, or post-processing [1].

Data harmonization in dMRI is attracting attention to overcome these problems [3]. One way to reduce uncontrolled variability is to eliminate the free-water signal [4]. Free-water elimination (FWE) uses a two-compartments tissue model composed by tissue (or parenchyma) and free-water [5]. Fitting the diffusion tensor in a two-compartments model is an ill-posed problem that has been solved using spatial regularization [6] or optimized acquisition protocols [7]. Harmonization of image resolution and diffusion directionality can be achieved by image quality transfer (IQT) with non-linear learninig algorithms, such as convolutional neural networks [8] or random forest [9]. IQT offers a new dimension in dMRI, enabling learning complex diffusion model on high quality data, to then transfer information captured in signal patterns to low quality data. However, this approach is limited by the availability of rich datasets.

We propose an new method for free-water elimination based on an artificial neural network (ANN), trained with synthetically generated data, that is independent of the number of diffusion shells (b-values) and can be applied retrospectively to any dMRI data. Instead of regularizing the FWE ill-posed inverse problem, we teach a non-parametric forward model to learn the mapping between partial volume contamination and free-water volume fraction from synthetic data. Besides, unlike IQT, our approach works only in the diffusion dimension, enabling an important simplification of the ANN model. We further show the advantages of FWE in glioblastoma cases: 1) a gain of statistical power through data harmonization, 2) complementary information of the tissue microstructure composition, and 3) better assessment of edema, tumor, and tumor infiltrated areas. The source code can be found in https://github.com/mmromero/dry.

2 Methods

Diffusion signal modeling: Following previous work on free-water elimination we modeled the diffusion signal of a single voxel, along the diffusion directions $(b, \boldsymbol{g})$, as the contribution of tissue and free-water compartments:

$$S(TE, b, \boldsymbol{g}) = S_0 \left(\hat{f}_t e^{\frac{-TE}{T_{2_t}}} S_t(b, \boldsymbol{g}) + \hat{f}_{fw} e^{\frac{-TE}{T_{2_{fw}}}} S_{fw}(b, \boldsymbol{g}) \right), \tag{1}$$

where b and $\boldsymbol{g}$ summarize the gradient effects; S_0 is a scaling factor proportional to the proton density; $\hat{f}_t$, $\hat{f}_{fw}$, T_{2_t}, and $T_{2_{fw}}$ are the volume fraction and T_2 values of tissue and free-water respectively. Since $T_{2_t} < T_{2_{fw}}$, measurements at different echo-times (TE) yield distinct contributions of tissue and free-water. Thus, disentangling the volume fractions from the T_2 effects requires measurements at least two different TEs [10]. However, in clinical routine only one TE is acquired simplifying Eq.1:

$$S(b, \boldsymbol{g}) = S_0 \left(f_t S_t(b, \boldsymbol{g}) + f_{fw} S_{fw}(b, \boldsymbol{g}) \right), \tag{2}$$

where the T_{2_i} and $\hat{f}_i$ effects are integrated in f_i, inducing a positive bias towards the new free-water volume fraction (f_{fw}) as TE increases. The volume

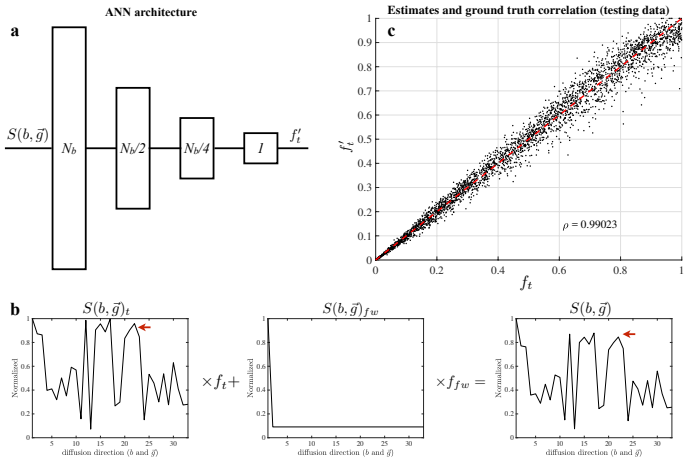

Fig. 1. Artificial neural network model. The ANN architecture (a). Training data was synthetically generated following Eq. 2 (b). Free-water partial volume contamination effects were visible (b, red arrows). We ran a correlation analysis for 3000 randomly generated samples (c) reaching a factor of 0.99.

fraction indexes are ratios relative to the signal contribution of each compartment and thus $f_{fw} + f_t = 1$.

Synthetic signal generation: The diffusion properties of free-water at body temperature are well characterized [5], presenting isotropic behavior and a diffusion coefficient $D_{fw} = 3 \times 10^{-3}$ mm^2/s, thus $S_{fw}(b, \boldsymbol{g}) = e^{-bD_{fw}}$. On the other hand, S_t is unknown since it depends on the tissue microstructure organization and the orientation of the diffusion gradients, $\boldsymbol{g}$. Thus, we modeled its behavior with a random variable, $S_t \in \mathbb{R}^{N_b}$, following an uniform distribution, $U(0, 1)$, where N_b is the number of diffusion measures, including non-diffusion-weighted volumes. Furthermore, we also represented the tissue volume fraction of a voxel, $f_t \in [0, 1]$, as a random uniform variable, $U(0, 1)$. Based on the prior knowledge of D_{fw}, the models of S_t and f_t, and knowing the diffusion protocol, it is possible to generate unlimited synthetic diffusion signals, $S(b, \boldsymbol{g})$, containing free-water partial volume effects (Eq. 2 and Fig. 1b).

ANN architecture and training: We designed a regression fully connected ANN capable of estimating the tissue volume fraction, f_t, directly from the diffusion signal $S(b, \boldsymbol{g})$ (Eq. 2). The input layer contained as many units as the number of acquired diffusion measures (including non-diffusion-weighted volumes), N_b, and a single output unit yielding the estimate of f_t. We compared ANN architectures containing from one to five hidden layers, finding an optimum in performance for two hidden layers with $N_b/2$ and $N_b/4$ respectively (Fig. 1a). To train the ANN we used 20000 synthetic signals generated as explained above (70% training, 15% validation, and 15% testing). Convergence for $N_b = 33$ (Fig. 1) was reached after nine epochs and 4.7 seconds in a consumers laptop (Apple

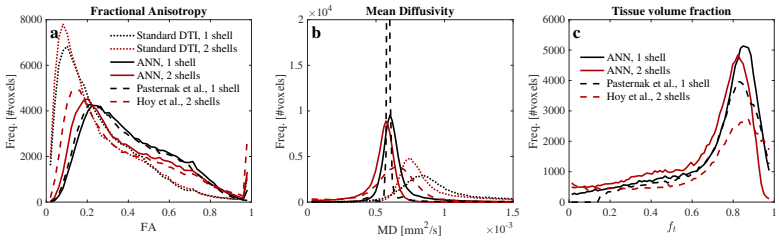

Fig. 2. Comparison of FWE with ANN and state of the art methods for two diffusion protocols. The correction effects on FA of ANN for one shell were equivalent to Pasternak's et al. algorithm (a), while ANN MD estimates were less over-regularized (b). Tissue volume fraction estimates were also in agreement although Pasternak's method failed to estimate $f_t < 0.18$ (c). The ANN for two shells and Hoy's et al. algorithm were in good agreement for FA (a) but larger differences were visible for MD and f_t (b and c). See the supplementary material for more information.

MacBook Pro, Intel Core i5, 8GB RAM; MATLAB, Mathworks, Natwick, MA). The training process depended on the diffusion protocol prescribed. Thus, we trained four networks to match the DWI data used in the experiments below.

3 Experiments and Results

Comparison with state of the art: Methods from Pasternak et al. [6] and Hoy et al. [7] are the state of the art for one and two shell acquisitions. For comparison we measured data from a volunteer in a GE 3T MR750w (GE Healthcare, Milwaukee, WI). The protocol comprised first, one diffusion weighted imaging (DWI) acquisition for 30 diffusion direction (b=500 s/mm^2) and two b=0 volume (N_b=32); and second a DWI for two shells (b=500 and 1000 s/mm^2) with 30 diffusion directions for each shell and four non-diffusion-weighted volumes (N_b=64). The data was processed with a pipeline including steps for: 1) head motion and eddy current corrections (FSL eddy); 2) denoising based on random matrix theory [11]; and 3) free-water elimination based on ANN, Pasternak's, and Hoy's methods (Fig. 2). The ANN results were comparable to those of the state of the art methods.

Data harmonization: The T_2 effects described in Eq.1 and Eq. 2 were investigated using data from a volunteer scanned in the same scanner as before. The protocol consisted of a DWI acquisition for 30 direction (b=1000 s/mm^2) and one non-diffusion-weighted volume (N_b = 31). This was repeated for seven equispaced TE = 74.9 – 134.9 ms. The data was processed as described before, but only ANN FWE was computed. For comparison two processing lines were created with and without ANN based FWE. Both were fitted with robust DTI (RESTORE) [12] to extract diffusion metrics.

The multi-echo diffusion data showed an increase of free-water (Fig. 3c) and its effects (Fig. 3a, larger low FA peak) with the TE, which agrees with the

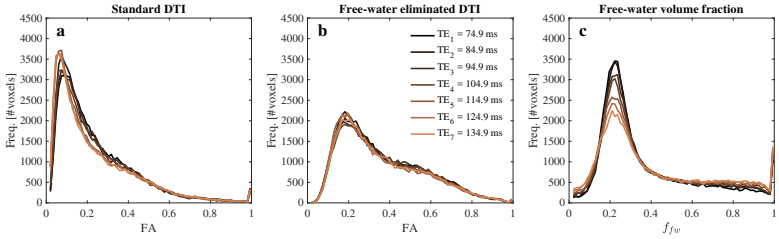

Fig. 3. Histogram comparison at several TEs. FA from standard DTI (a) showed larger variability across TEs for FA < 0.4, than the free-water corrected (b). The tissue volume fraction estimates are influenced by T_2 decay (Eq. 1) and thus sensitive to TE (c). The free-water elimination step has a TE harmonization effect on the diffusion signal (b), shifting the TE variability into the volume fraction estimate (c).

two-compartments tissue model (Eq. 1) accounting for T_2 effects, simplified in Eq. 2. Multi-center studies are often carried out in data acquired with heterogeneous protocols. The prescribed TEs are a source of variability that mostly depend on the gradient strength of the scanner and the image resolution. Data harmonization is important to remove uncontrolled variability and achieve a good statistical power. Free-water elimination plays a double role. First, it accounts for T_2 effects in the f_i, shifting this variability from the diffusion metrics to the volume fraction estimates (Fig. 3). And second, it removes the "diffusion isotropic noise" from the signal showing the actual tissue anisotropy, eliminating the variability induced by the presence of free-water.

Glioblastoma analysis: Data from 25 patients affected by glioblastoma (IDH wild-type, WHO 2016 classification) were provided by the Department of Neuroradiology, Klinikum rechts der Isar der Technischen Universität München, Munich, Germany. All patients are part of a prospective glioma database, approved by the local ethics committee, and gave written informed consent. They were scanned in a 3T whole-body scanner (Achieva, Philips Medical Systems, Best, The Netherlands). The protocol included DWI for 32 directions (b=800 s/mm^2) and one non-diffusion-weighted volume ($N_b = 33$). Furthermore, T_2 turbo spin echo (T2w), T_2-FLAIR, and T_1 contrast enhanced (CE-T1w) were acquired. The DWI data was processed as described before, and T2w, CE-T1w, and FLAIR volumes were registered to the DWI space (Fig. 4).

Tissue and free-water volume fraction estimates: The free-water and tissue maps computed with ANN (Fig. 4d and h) showed tumor and edema areas that were in agreement with well established methods: T2w, CE-T1w, and FLAIR (Fig. 4e, f, and g). The estimation of tissue and free-water volume fraction maps is an important feature of FWE. They provide complementary information of the underlying tissue organization. Cytotoxic edema and necrosis areas that are not distinguishable can be better identified with the knowledge of the amount of tissue in the voxel (Fig. 4d, e, f, g, and h, light-blue arrows). Furthermore, in clinical routine tumor delineation is based on CE-T1w hyper-intensities (Fig. 4f

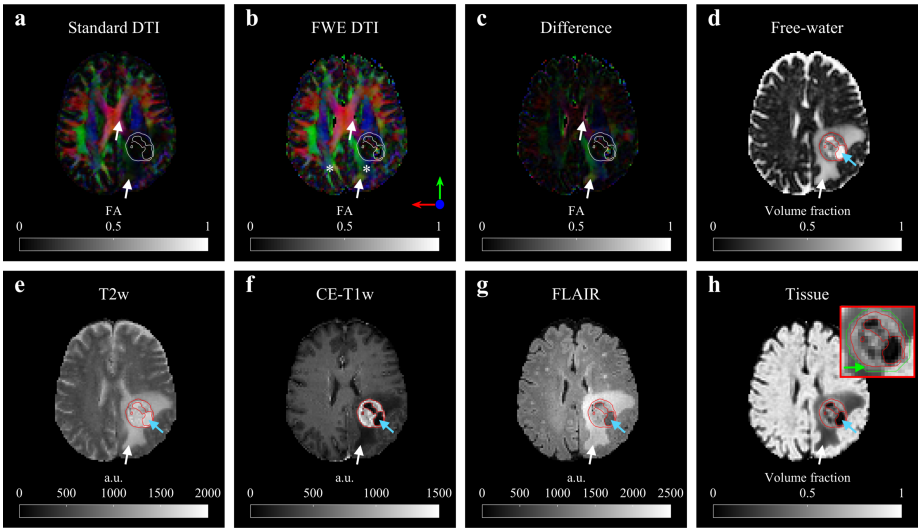

Fig. 4. Comparison of metrics and contrasts for one patient. Fractional anisotropy from standard DTI (a) showed a dimmed region corresponding to edema (white arrows). This area was recovered after free-water elimination (b and c). We observed alterations of the white matter integrity compared to the NAWM (b, white asterisks). Free-water (d) and tissue (h) volume fraction maps were estimated by the ANN. Edema regions were well defined and distinguishable from the tumor (red contour). Pools compatible with cytotoxic edema were observable inside the tumor (light-blue arrows). These findings agreed with the observations based on T2w (e), CE-T1w (f), and FLAIR (g). Extended tumor infiltration was derived from the comparison of CE-T1w and tissue volume fraction map (h, green arrow and contour).

red contour). When this is compared with tissue volume fraction maps (Fig. 4h zoomed area), we observed an increased tumor region of up to four millimeters that is compatible with tumor infiltration. This agrees with the radiated area after resection (Fig. 4h, green arrow and contour).

Fractional anisotropy recovery: The comparison between standard and FWE FA maps (Fig. 4a and b) exhibited a recovery of the anisotropic information in the edema region and around the ventricles (Fig. 4c, white arrows). The elimination of the isotropic compartment from the diffusion signal leads to a recovery of the tissue anisotropy captured by the protocol, leading to an enhancement of the FA maps, especially in areas with large partial volume contamination like edema and the border of the ventricles (Fig. 4a, b, and c, white arrows). The correction of the FA maps provides new information of the tissue microstructure integrity hidden by the edema (Fig. 4b asterisks).

Edema and infiltration unmixing: To assess the impact of FWE in edema, tumor, and tumor infiltrated areas, regions of interests (ROI) were defined by a neuroradiologist for each subject using FLAIR, T2w, CE-T1w, f_t, and FWE

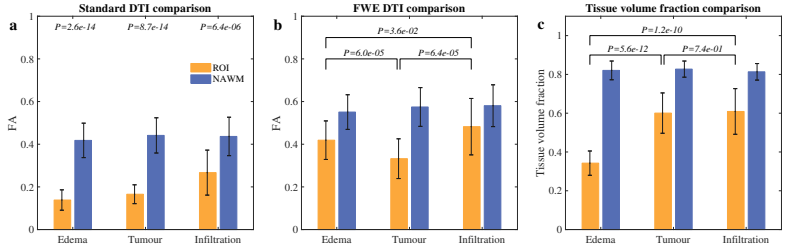

Fig. 5. Edema, tumor, and tumor infiltrated regions differentiation. The FA values for standard DTI (a) were statistically different ($\alpha = 0.01$) between NAWM areas. After free-water elimination (b) FA values in edema and tumor infiltrated areas were significantly larger than those for tumor (family-wise error = 0.03), indicating a better organized tissue microstructure. Complementary, the tissue volume fractions in tumor and tumor infiltrated regions were statistically larger than in edema areas, suggesting that the loss in FA in edema was mostly due to free-water infiltration.

FA maps (Fig. 4). To minimize the influence of outliers we used the median for each ROI, and ran t-test comparison for FA and tissue volume fraction values across subjects for the three type of ROIs (Fig. 5). For reference, extra ROIs were drawn in normal appearing white mater (NAWM) mostly contralateral.

Comparison of NAWM with tumor and edema areas for the 25 patients showed a statistically significant difference ($\alpha = 0.01$) in FA for standard DTI (Fig. 5a). Tumor infiltration and edema are the driving factors behind the loss in FA. After free-water elimination we compared FWE FA (Fig. 5b) and tissue volume fraction (Fig. 5c) in edema, tumor and tumor infiltrated areas (family-wise error = 0.03). Significantly larger FA was found in edema and tumor infiltrated areas compared to tumor regions. While, tissue volume fraction in edema was statistically lower than in tumor infiltrated and tumor sections.

We hypothesize that the combination of FWE FA and tissue volume fraction yields a better understanding of tissue microstructure integrity (Fig. 5). High FA and low tissue volume fraction might indicate well organized microstructure infiltrated by free-water (vasogenic edema). Low FA and high tissue volume fraction is compatible with the unstructured cellularity found in tumors. Finally, areas with high FA and tissue volume fraction might be caused by tumor infiltration in highly structured white matter bundles.

Discussion

The presented ANN model combines simplicity with high accuracy. We introduce for the first time an ANN design capable of learning partial volume effect features from synthetic data, and reach comparable results with the state of the art methods but at least 55-fold faster. Besides, our approach, unlike [6] is voxel-based, avoiding blurring artifacts induced by the use of patch based

regularization, and can be applied to any diffusion protocol beyond DTI. The robustness of our approach was shown with 25 patients, 2 volunteers, 4 protocols, and 2 scanners from different manufacturers. We attribute these results to the good understanding of the physical signal model mimicked by the ANN.

The addition of free-water elimination in processing pipeline extracts more information from the data, which has a potential benefit for glioblastoma patients in three aspects: diagnosis, surgical planning, and guided radiotherapy. The diagnosis potentially improves with the quantification of the free-water volume fraction map, yielding the severity of the vasogenic edema. The precision of the surgical planning benefits from the corrected FA maps in edema areas providing a better definition of white matter fiber bundles and limiting the resection of healthy tissue. Finally, guided radiotherapy profits from identification of tumor infiltrated areas.

Acknowledgments

The authors want to thank Dr. Ofer Pasternak for his support in the comparison of the methods. This work was supported by the TUM Institute of Advanced Study, funded by the German Excellence Initiative, and the European Commission (Grant Agreement Number 605162).

References

1. A.S. Field. Diffusion imaging in brain tumors. In D.K. Jones, editor, *Diffusion MRI*, chapter 33, pages 547–563. Oxford University Press, 2010.
2. S. Bette et al. Local Fractional Anisotropy Is Reduced in Areas with Tumor Recurrence in Glioblastoma. *Radiology*, 283(2):499–507, 2017.
3. Z. Eaton-Rosen et al. Beyond the Resolution Limit: Diffusion Parameter Estimation in Partial Volume. *MICCAI*, pages 605–612, 2016.
4. C. Metzler-Baddeley et al. How and how not to correct for CSF-contamination in diffusion MRI. *Neuroimage*, 59(2):1394–1403, 2012.
5. C. Pierpaoli and D.K. Jones. Removing CSF Contamination in Brain DT-MRIs by Using a Two-Compartment Tensor Model. In *ISMRM, Kyoto*, page 1215, 2004.
6. O. Pasternak et al. Free Water Elimination and Mapping from Diffusion MRI. *Magn. Reson. Med.*, 730:717–730, 2009.
7. A.R. Hoy et al. Optimization of a Free Water Elimination Two-Compartment Model for Diffusion Tensor Imaging. *Neuroimage*, (103):323–333, 2014.
8. R. Tanno et al. Bayesian image quality transfer with CNNs: Exploring uncertainty in dMRI super-resolution. volume 10433 LNCS, pages 611–619, 2017.
9. D.C. Alexander et al. Image quality transfer and applications in diffusion MRI. *Neuroimage*, 152(March):283–298, 2017.
10. M. Molina-Romero et al. A diffusion model-free framework with echo time dependence for free-water elimination and brain tissue microstructure characterization. *Magn. Reson. Med.*, mar 2018.
11. J. Veraart et al. Denoising of diffusion MRI using random matrix theory. *Neuroimage*, 142:394–406, nov 2016.
12. L. Chang et al. Restore: Robust estimation of tensors by outlier rejection. *Magnetic Resonance in Medicine*, 53(5):1088–1095, 2005.